

Identification of ferrimagnetic orbitals preventing spinel degradation by charge ordering in $\text{Li}_x\text{Mn}_2\text{O}_4$

Hasnain Hafiz^{1,*}, Kosuke Suzuki,² Bernardo Barbiellini,^{3,1} Yuki Orikasa,⁴ Stanislaw Kaprzyk,^{5,1,†} Naruki Tsuji,⁶ Kentaro Yamamoto,⁷ Ayumu Terasaka,² Kazushi Hoshi,² Yoshiharu Uchimoto,⁷ Yoshiharu Sakurai,⁶ Hiroshi Sakurai,² and Arun Bansil^{1,‡}

¹*Department of Physics, Northeastern University, Boston, Massachusetts 02115, USA*

²*Faculty of Science and Technology, Gunma University, Kiryu, Gunma 376-8515, Japan*

³*School of Engineering Science, LUT University, FI-53851 Lappeenranta, Finland*

⁴*Department of Applied Chemistry, Ritsumeikan University, Kusatsu, Shiga 525-8577, Japan*

⁵*Faculty of Physics and Applied Computer Science, AGH University of Science and Technology, aleja Mickiewicza 30, Krakow 30-059, Poland*

⁶*Japan Synchrotron Radiation Research Institute, SPring-8, Sayo, Hyogo 679-5198, Japan*

⁷*Graduate School of Human and Environmental Studies, Kyoto University, Sakyo-ku, Kyoto 606-8501, Japan*



(Received 2 May 2019; published 4 November 2019)

Spinel $\text{Li}_x\text{Mn}_2\text{O}_4$ is a key cathode material that is used extensively in commercial Li-ion batteries. A challenge with this material has been that the capacity of the battery fades with cycling, an effect that can be traced to the presence of an antiferromagnetic insulator phase in the fully lithiated LiMn_2O_4 (LMO) and the associated charge disproportionation that drives distortions of the MnO_6 octahedra. Here, by combining x-ray magnetic Compton scattering experiments with parallel first-principles computations, we show that the antiferromagnetic phase of LMO is surrounded by a robust ferrimagnetic metallic phase, which becomes stable when even a small amount of Li is removed from or added to the charge-ordered LMO. In this surprising ferrimagnetic state, charge-ordering and octahedral distortions are found to be strongly suppressed. We identify the nature of the ferrimagnetic orbitals involved through theoretical and experimental analyses of the magnetic Compton scattering spectra.

DOI: [10.1103/PhysRevB.100.205104](https://doi.org/10.1103/PhysRevB.100.205104)

I. INTRODUCTION

Spinel $\text{Li}_x\text{Mn}_2\text{O}_4$ is an attractive cathode material for rechargeable batteries [1,2] because it is less expensive and environmentally more friendly than lithiated cobalt and nickel oxides. Unfortunately, the lithiated ($x = 1$) compound LiMn_2O_4 (LMO) suffers from the problem of capacity fading due to a structural phase transition [3,4]. Above room temperature, LMO assumes the cubic structure of the normal spinel in which lithium ions occupy tetrahedral positions, with the manganese ions located only at the octahedral positions. A decrease in the temperature to around 283 K produces the famous metal-insulator (Verwey) transition [5], which is associated with the distortion of the MnO_6 octahedra. This structural transformation limits the application of LMO as a cathode material [6]. The Verwey transition also drives the onset of long-range antiferromagnetic (AFM) order below the Curie temperature of 65 K [7], which is also supported by first-principles calculations [8]. Geometric frustration of the AFM order in the spinel structure [9] leads to complex potential energy landscapes that exhibit multiple magnetic phase transitions [10] whose nature remains unclear.

In this study, we explore magnetic properties of spinel $\text{Li}_x\text{Mn}_2\text{O}_4$ on a first-principles basis by exploiting recent advances in constructing exchange-correlation functionals. Specifically, we employ the strongly constrained and appropriately normed (SCAN) functional [11], which has proven especially accurate for investigating the electronic, geometric, and magnetic structures of elemental manganese [12], MnO_2 polymorphs [13], $3d$ perovskite oxides [14], oxides superconductors [15–17], and layered lithium intercalated transition-metal oxides [18]. Parallel magnetic Compton scattering experiments on LMO samples are also reported over a wide range of Li concentrations varying from unlithiated ($x = 0$) to overlithiated ($x = 1.079$) $\text{Li}_x\text{Mn}_2\text{O}_4$. Our analysis reveals that ferrimagnetism competes with the AFM order in LMO and leads to ferrimagnetic (FIM) moments even for slight departures from stoichiometry ($x = 1$). Liu *et al.* [8] report that the AFM ordering is responsible for triggering changes in the Mn valence and driving Jahn-Teller distortions. The FIM phase we have found here, however, suppresses the octahedral distortions, which are responsible for cathode degradation. We show how the magnetic state associated with this puzzling FIM phase can be visualized through an analysis of our magnetic Compton spectra.

Compton scattering, which refers to inelastic x-ray scattering in the deeply inelastic regime, provides a direct probe of the ground-state momentum density $\rho(\mathbf{p})$ of the many-body electronic system through a measurement of the so-called Compton profile, $J(p_z)$, where p_z is the momentum transferred in the scattering process [19,20]. High-resolution

*hafiz.h@husky.neu.edu; Present address: Department of Mechanical Engineering, Carnegie Mellon University, Pittsburgh, PA 15213, USA.

†Deceased

‡ar.bansil@northeastern.edu

x-ray Compton scattering studies have revealed that the orbital involved in the lithium insertion/extraction process in $\text{Li}_x\text{Mn}_2\text{O}_4$ is mainly the oxygen $2p$ orbital [21]. Although the oxygen $2p$ orbitals thus dominate the redox process, magnetic properties of the material are controlled by manganese $3d$ orbitals. Here, we use magnetic Compton scattering (MCS) to explore how the manganese $3d$ states evolve with Li intercalation and how their magnetism drives the performance of the battery.

In an MCS experiment, one measures the magnetic Compton profile (MCP) [19], J_{mag} , which can be expressed in terms of a double integral of the spin-dependent electron momentum density, $\rho_{\text{mag}}(\mathbf{p})$, as

$$J_{\text{mag}}(p_z) = \iint \rho_{\text{mag}}(\mathbf{p}) dp_x dp_y. \quad (1)$$

Here, $\rho_{\text{mag}}(\mathbf{p}) = \rho_{\uparrow}(\mathbf{p}) - \rho_{\downarrow}(\mathbf{p})$, where $\rho_{\uparrow}(\mathbf{p})$ and $\rho_{\downarrow}(\mathbf{p})$ are the momentum densities of up-spin (majority) and down-spin (minority) electrons, respectively. The area under the magnetic Compton profile $J_{\text{mag}}(p_z)$ yields the total magnetic spin moment. Therefore, MCS experiments require a strong magnetic field and a net total magnetic moment in the sample. In this way, MCS allows access to magnetic electrons in materials, and its potential in this regard was recognized quite early in the field [22,23]. The technique has proven especially successful in extracting occupation numbers of $3d$ Mn orbitals in bilayer manganites [24,25], and recent MCS studies have revealed fine details of the magnetic orbitals in a number of materials [26–28].

II. MATERIALS AND METHODS

A. Magnetic Compton experiments

The MCS experiments were carried out at 10 K on beamline BL08W at SPring-8, Japan [29,30]. Elliptically polarized x rays emitted from an elliptical multipole wiggler were monochromatized to 183 keV by a bent Si 620 crystal. Energy spectra of Compton-scattered x rays from the sample at a scattering angle of 178° were measured using a ten-segmented Ge solid-state detector with an external magnetic field of 25 kOe. The estimated momentum resolution is 0.50 a.u. full width at half-maximum. The spherically averaged profile $J_{\text{mag}}(p)$ was extracted from the difference between two spectra taken under the same experimental conditions with alternating directions of magnetization of the sample, aligned by an external magnetic field [19]. The observed spectra were corrected for the energy-dependent scattering cross section, the efficiency of the detector, and the absorption of the sample.

Polycrystalline samples of $\text{Li}_x\text{Mn}_2\text{O}_4$ ($x = 0.41, 0.50, 0.92, \text{ and } 1.08$) were prepared by chemical lithium extraction following the method reported previously [21]. The compositions were determined by inductively coupled plasma (ICP) measurements. X-ray powder diffraction analyses confirmed spinel phases and the increase of the lattice constant with increasing x over the range $x = 0$ – 1 as observed previously [21]. Total magnetic moments were obtained from SQUID magnetometer (MPMS5-SW, Quantum Design, Inc.) measurements.

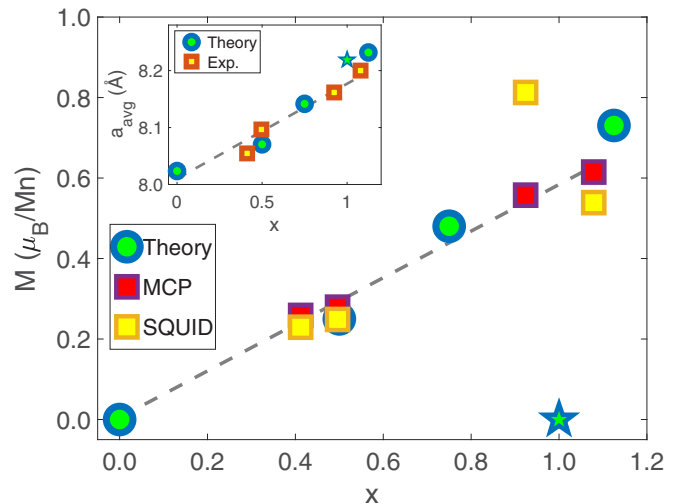


FIG. 1. FIM phase in $\text{Li}_x\text{Mn}_2\text{O}_4$. Magnetic moments for various lithium concentrations x obtained via magnetic Compton scattering (red squares) and SQUID (yellow squares) measurements are compared with the corresponding theoretical predictions (green circles). The disappearance of the total magnetic moment at $x = 1$ is highlighted by the star symbol. The inset shows how the experimental and theoretical values of the average lattice constant vary with x and approximately follow a linear behavior consistent with Vegard's law.

B. First-principles calculations

First-principles calculations were performed using the pseudopotential projector augmented-plane-wave method [31] as implemented in the Vienna *Ab-Initio* Simulation Package (VASP) [32,33], with a kinetic energy cutoff of 600 eV for the plane-wave basis set. Computations were carried out using both the generalized gradient approximation (GGA) [34,35] and the recently constructed strongly constrained and appropriately normed (SCAN) meta-GGA [11] exchange-correlation functional. A $4 \times 4 \times 4$ Γ -centered k -point mesh was used to sample the Brillouin zone of a primitive spinel unit cell (containing eight formula units with 32 oxygen atoms). Equilibrium positions of all atoms were calculated via structural optimization, where the internal degrees of freedom, along with the shape and volume of the unit cell, were allowed to vary until the residual forces per atom were less than $0.005 \text{ eV}/\text{\AA}$. We obtained spin momentum densities, $\rho_{\text{mag}}(\mathbf{p})$, and the spherical Compton profiles $J_{\text{mag}}(p)$ of the valence electrons using Kohn-Sham orbitals following the method of Makkonen *et al.* [36]. This scheme was used recently to study the Compton profile of lithium iron phosphate (LiFePO_4) [37], which is as an exemplar cathode battery material [38,39].

III. RESULTS AND DISCUSSIONS

A. Ferrimagnetic phase

Figure 1 highlights the evolution of the magnetic moment in $\text{Li}_x\text{Mn}_2\text{O}_4$ for Li concentrations varying from zero to around 1.1 per formula unit. The experimental Compton magnetic moment is seen to follow a linear behavior as shown by the gray dashed line. The AFM state (zero average moment) is realized in the end compounds MnO_2 and

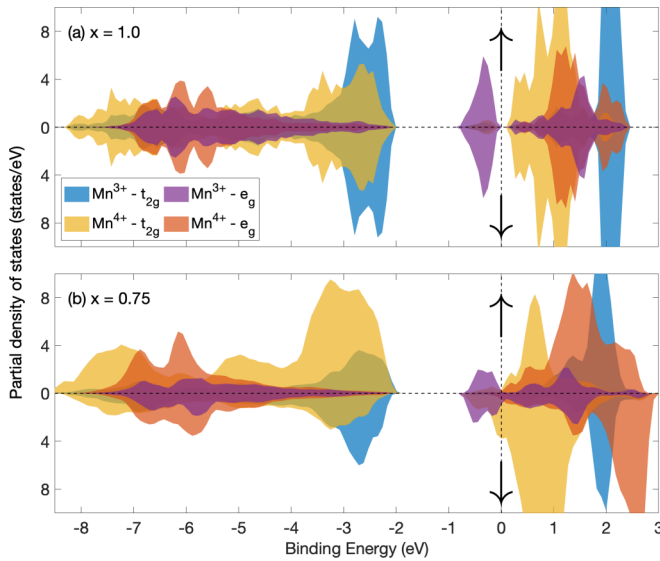


FIG. 2. Computed spin-dependent partial density of states (PDOS) associated with the e_g and t_{2g} orbitals of Mn^{3+} and Mn^{4+} ions in $\text{Li}_x\text{Mn}_2\text{O}_4$ for Li concentrations (a) $x = 1.0$ and (b) $x = 0.75$. See panel (a) for the meaning of lines of various colors. The vertical dashed line marks the Fermi energy (E_F). Up and down arrows indicate the contributions of spin-up and -down PDOS, respectively.

LiMn_2O_4 , but the system assumes a ferrimagnetic (FIM) state with a net nonzero moment at other compositions, including the overdischarged regime of $x > 1$. The moments obtained via SQUID measurements are in good accord with those obtained from MCS experiments. Some differences are to be expected since MCS measures only the spin moment [22] while the SQUID couples to the total moment, which includes the orbital component of the magnetic moment. Notably,

anomalous behavior of the magnetic moment near the Verwey transition has been reported previously [40]. Our theoretical moments (green circles) are in reasonable accord with the corresponding experimental results (red and yellow squares). Some excursion from linearity in theoretical moments could be due to the small size of the simulation cell used in computations. In fact, Korringa-Kohn-Rostoker-coherent-potential-approximation (KKR-CPA) [41,42] calculations show that the spin moment on Mn atoms increases linearly with increasing x if the system is described by a spin-glass-like behavior with randomly oriented Mn moments [21]. Moreover, the strengthening of Mn moments with Li insertion is consistent with muon-spin-rotation experiments [43]. However, the random-alloy model [21] underlying the KKR-CPA scheme cannot be expected to capture the AFM charge-ordered state at $x = 1$.

B. Charge, spin, and magnetic configuration

The SCAN functional used in this study successfully localizes Mn $3d$ electrons by filling $3d_{z^2}$ orbitals, and it results in the coexistence of Mn^{3+} and Mn^{4+} in LiMn_2O_4 . Figure 2, which presents our spin-dependent partial density of states (PDOS) in $\text{Li}_x\text{Mn}_2\text{O}_4$, shows that e_g orbitals of some Mn atoms split upon lithium intercalation. The Mn $3d_{z^2}$ levels move to lower energies and become filled, and eventually open a band gap of about 0.1 eV at $x = 1$. For $0 < x < 1$, the system is metallic due to the partial occupation of the Mn $3d_{z^2}$ bands. At $x = 1$, the ground state is found to be an AFM charge-ordered state with alternating AFM Mn^{3+} layers and FM Mn^{4+} layers with spins along the (001) direction as illustrated in Fig. 3(a). FIM states appear as soon as Li atoms are removed from or added to the unit cell. A stable FIM configuration for $x = 0.75$ is shown in Fig. 3(b). In this phase, the spin of the t_{2g} electrons is not compensated

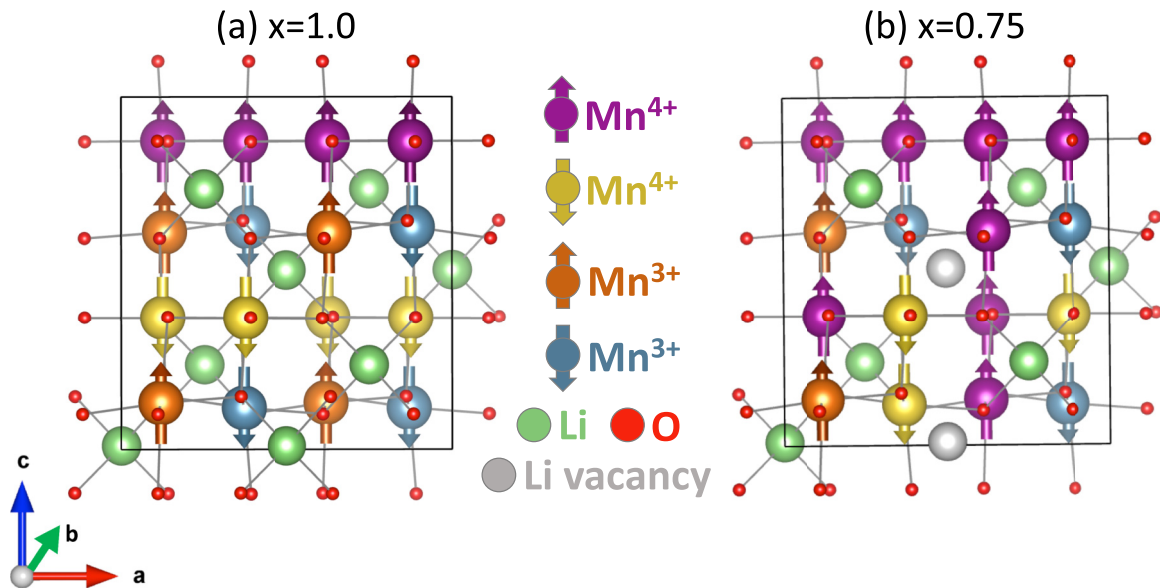


FIG. 3. Schematics of magnetic configurations of $\text{Li}_x\text{Mn}_2\text{O}_4$ for lithium concentrations $x = 1$ and 0.75 . Charge-ordering is prominent for the $x = 1$ phase with an overall AFM configuration (a). As soon as the Li ions are removed [see (b)], charge-ordering becomes unstable, and it results in partial ordering, spin-flipping, and a reduction of the average local magnetic moment per Mn atom. This induces ferrimagnetism at $x = 0.75$, which is seen also in the PDOS of Fig. 2(b).

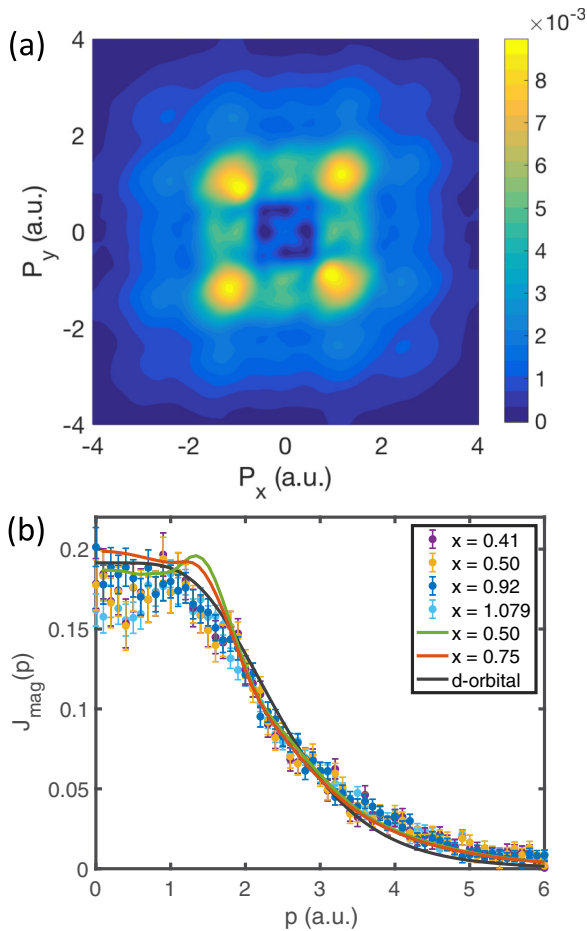


FIG. 4. Compton profiles and visualization of the magnetic orbitals. (a) Theoretical 2D momentum density map for projection along (001) for $x = 0.75$. (b) Experimental (scatter plots with error bars) and theoretical (solid lines) spherically averaged magnetic Compton profiles. The gray solid line represents the atomic d -orbital Compton profile, which is solved analytically using normalized Slater-type orbitals. All the profiles are normalized to 1.

according to the PDOS shown in Fig. 2(b), and therefore these electrons produce a net magnetic moment. Interestingly, we found a similar magnetic PDOS for the overlithiated phase $x = 1.125$ where the Mn t_{2g} state is partially compensated, and hence it is mainly responsible for the magnetic moment as shown in Fig. S1(a) of the supplemental material [44]. In general, SCAN is able to describe complex configurations of competing stripe and magnetic phases in the cuprates [17], and it also produces a small distortion from the $Fd3m$ cubic symmetry of $\text{Li}_x\text{Mn}_2\text{O}_4$ at $x = 0.5$ [see Figs. S1(b) and S3(b) in the supplemental material [44]], which is consistent with the recent experimental results of Bianchini *et al.* [45]. In sharp contrast to the preceding SCAN-based results, the GGA functional [46] fails to produce the insulating AFM state of LiMn_2O_4 and the associated charge disproportionation on Mn atoms that drives local Jahn-Teller distortions [8] of the MnO_6 octahedra. Notably, the theoretical lattice parameters obtained via SCAN are in good agreement with the corresponding experimental values as shown in the inset of Fig. 1.

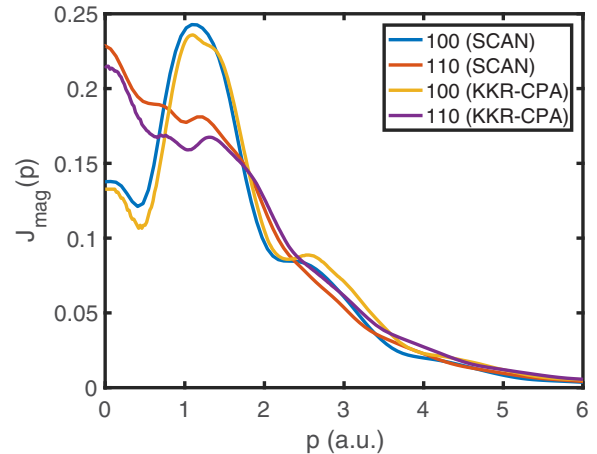


FIG. 5. Directional Magnetic Compton profiles along the (100) and (110) directions. The low-momentum contributions mainly come from the (110) directions, which contribute significantly to the spherical average in Fig. 4. The SCAN results show good agreement with the KKR-CPA results for the FIM phase.

C. Magnetic orbitals and Compton profiles

Electronic states in momentum space preserve their individual angular dependencies, which facilitates the detection of particular states [47]. Thus, the projection of the theoretical 3D spin-polarized electron momentum density $\rho_{\text{mag}}(\mathbf{p})$ along the (001) direction at $x = 0.75$ given in Fig. 4(a) determines the nature of the electronic states producing the FIM solution. Clearly, the angular dependence of $\rho_{\text{mag}}(\mathbf{p})$ is dominated by the t_{2g} character of the $3d$ Mn electrons [48]. This spin momentum result is consistent with our previous observation that the t_{2g} electrons are not compensated according to Fig. 2(b) of the PDOS. Based on these robust arguments, one can conclude that the FIM orbitals have mostly t_{2g} character. Figure 4(b) presents the measured and calculated spherically averaged MCPs for various lithium concentrations, x . For all values of x , the shapes of the MCPs are quite similar, the main difference being the area under the profile, which gives the total spin magnetic moment. As we noted already, the spin magnetic moment follows a linear behavior for all lithium concentrations with the exception of the $x = 1$ compound where the moment vanishes. The agreement between theory and experiment in Fig. 4(b) is considered very good when we keep in mind the delicate nature of the MCP. The shape of the experimental $J_{\text{mag}}(p)$ is also similar to that of the Compton profile from a manganese $3d$ atomic orbital [49] since the manganese t_{2g} orbitals undergo little hybridization with the $2p$ orbital of oxygen [21]. Figure 5 shows a comparison of the directional Compton profiles between the KKR-CPA and SCAN calculations. As mentioned above, our KKR-CPA calculations describe a spin-glass-like behavior with randomly oriented Mn moments embedded in a perfect cubic spinel structure. Therefore, the agreement between the two methods indicates that SCAN can successfully capture the almost cubic FIM spin-glass phase. Thus, the Jahn-Teller distortions obtained within SCAN are strongly suppressed if the electrons occupy the FIM orbitals visualized in Fig. 4(a). As shown by our magnetic Compton scattering experiments, the application of an

external field promoting the FIM phase and the associated orbitals can serve as a basis for preventing Jahn-Teller distortions.

IV. CONCLUSIONS

We have shown that a fundamental understanding of the role of magnetic electrons in Li-ion battery materials can be obtained via magnetic Compton scattering experiments and first-principles calculations. Specifically, the magnetic Compton profiles of a Li-Mn-O system at different lithium concentrations have been analyzed to unfold the underlying magnetic transitions in terms of the spin-moment contribution of the Mn $3d$ orbitals. The calculated total spin moments are in good agreement with the corresponding experimental values. The present analysis demonstrates that the Mn $3d$ magnetic electrons have mainly t_{2g} symmetry, and therefore these electrons prevent Jahn-Teller distortions promoted by the e_g character. Our study explains the intimate connection between the charge, spin, and lattice degrees of freedom and their role in the bonding of the MnO_6 octahedra [50] in the spinel battery materials. Although our present analysis is based on spherically averaged experimental MCPs, it will be interesting to consider directional MCPs from single-crystal samples to gain further insight into the nature of the connection between the octahedral bonds and magnetism. Electron transfer during the lithiation and delithiation processes is shown to involve octahedral units whose distortion can be

affected by temperature and magnetic field. In this way, the nature of the octahedral bonds and magnetism is connected with the electrochemical performance of the battery materials.

ACKNOWLEDGMENTS

We thank Dr. M. Ito for technical support in connection with magnetic Compton scattering experiments. K.S. was supported by a Grant-in-Aid for Young Scientists (B) (No. 15K17873) from the Ministry of Education, Culture, Sports, Science, and Technology (MEXT), Japan, and the work at JASRI was partially supported by the Japan Science and Technology Agency. Compton scattering experiments were performed with the approval of JASRI (Proposals No. 2014B1335 and 2015B1171). SQUID measurement was performed with the approval of Gunma University-Industry Collaboration and Intellectual Property Strategy Center (Proposal 2017). The work at Northeastern University was supported by the U.S. Department of Energy (DOE), Office of Science, Basic Energy Sciences Grant No. DE-FG02-07ER46352 (core research), and benefited from Northeastern University's Advanced Scientific Computation Center (ASCC), the NERSC supercomputing center through DOE Grant No. DE-AC02-05CH11231, and support (testing efficacy of advanced functionals) from the DOE EFRC: Center for Complex Materials from First Principles (CCM) under Grant No. DE-SC0012575.

H.H. and K.S. contributed equally to this work.

-
- [1] M. M. Thackeray, W. I. F. David, P. G. Bruce, and J. B. Goodenough, Lithium insertion into manganese spinels, *Mater. Res. Bull.* **18**, 461 (1983).
- [2] M. S. Islam and C. A. J. Fisher, Lithium and sodium battery cathode materials: Computational insights into voltage, diffusion and nanostructural properties, *Chem. Soc. Rev.* **43**, 185 (2014).
- [3] Y. Ein-Eli, R. C. Urian, W. Wen, and S. Mukerjee, Low temperature performance of copper/nickel modified LiMn_2O_4 spinels, *Electrochim. Acta* **50**, 1931 (2005).
- [4] Z. Zhuo, P. Olalde-Velasco, T. Chin, V. Battaglia, S. J. Harris, F. Pan, and W. Yang, Effect of excess lithium in LiMn_2O_4 and $\text{Li}_{1.15}\text{Mn}_{1.85}\text{O}_4$ electrodes revealed by quantitative analysis of soft X-ray absorption spectroscopy, *Appl. Phys. Lett.* **110**, 093902 (2017).
- [5] J. Rodríguez-Carvajal, G. Rousse, C. Masquelier, and M. Hervieu, Electronic Crystallization in a Lithium Battery Material: Columnar Ordering of Electrons and Holes in the Spinel LiMn_2O_4 , *Phys. Rev. Lett.* **81**, 4660 (1998).
- [6] K. Ragavendran, H. Xia, P. Mandal, and A. K. Arof, Jahn-Teller effect in LiMn_2O_4 : Influence on charge ordering, magnetoresistance and battery performance, *Phys. Chem. Chem. Phys.* **19**, 2073 (2017).
- [7] I. Tomeno, Y. Kasuya, and Y. Tsunoda, Charge and spin ordering in LiMn_2O_4 , *Phys. Rev. B* **64**, 094422 (2001).
- [8] W.-W. Liu, D. Wang, Z. Wang, J. Deng, W.-M. Lau, and Y. Zhang, Influence of magnetic ordering and Jahn-Teller distortion on the lithiation process of LiMn_2O_4 , *Phys. Chem. Chem. Phys.* **19**, 6481 (2017).
- [9] A. S. Wills, N. P. Raju, and J. E. Greedan, Low-temperature structure and magnetic properties of the spinel LiMn_2O_4 : A frustrated antiferromagnet and cathode material, *Chem. Mater.* **11**, 1510 (1999).
- [10] X. K. Zhang, J. J. Yuan, Y. M. Xie, Y. Yu, F. G. Kuang, H. J. Yu, X. R. Zhu, and H. Shen, Phase coexistence and exchange-bias effect in LiMn_2O_4 nanorods, *Phys. Rev. B* **97**, 104405 (2018).
- [11] J. Sun, A. Ruzsinszky, and J. P. Perdew, Strongly Constrained and Appropriately Normed Semilocal Density Functional, *Phys. Rev. Lett.* **115**, 036402 (2015).
- [12] A. Pulkkinen, B. Barbiellini, J. Nokelainen, V. Sokolovskiy, D. Baygutlin, O. Miroshkina, M. Zagrebin, V. Buchelnikov, C. Lane, R. S. Markiewicz, A. Bansil, J. Sun, and E. Lähderanta, Correlation in noncollinear antiferromagnetic α -Mn, *arXiv:1904.10291*.
- [13] D. A. Kitchaev, H. Peng, Y. Liu, J. Sun, J. P. Perdew, and G. Ceder, Energetics of MnO_2 polymorphs in density functional theory, *Phys. Rev. B* **93**, 045132 (2016).
- [14] J. Varignon, M. Bibes, and A. Zunger, Origin of band gaps in $3d$ perovskite oxides, *Nat. Commun.* **10**, 1658 (2019).
- [15] J. W. Furness, Y. Zhang, C. Lane, I. G. Buda, B. Barbiellini, R. S. Markiewicz, A. Bansil, and J. Sun, An accurate first-principles treatment of doping-dependent electronic structure of high-temperature cuprate superconductors, *Commun. Phys.* **1**, 11 (2018).
- [16] C. Lane, J. W. Furness, I. G. Buda, Y. Zhang, R. S. Markiewicz, B. Barbiellini, J. Sun, and A. Bansil, Antiferromagnetic ground state of La_2CuO_4 : A parameter-free *ab initio* description, *Phys. Rev. B* **98**, 125140 (2018).

- [17] Y. Zhang, C. Lane, J. W. Furness, B. Barbiellini, R. S. Markiewicz, A. Bansil, and J. Sun, Landscape of competing stripe and magnetic phases in cuprates, [arXiv:1809.08457](https://arxiv.org/abs/1809.08457).
- [18] A. Chakraborty, M. Dixit, D. Aurbach, and D. T. Major, Predicting accurate cathode properties of layered oxide materials using the SCAN meta-GGA density functional, *npj Comput. Mater.* **4**, 60 (2018).
- [19] M. J. Cooper, P. E. Mijnders, N. Shiotani, N. Sakai, and A. Bansil, *X-Ray Compton Scattering* (Oxford University Press, Oxford, 2004).
- [20] I. G. Kaplan, B. Barbiellini, and A. Bansil, Compton scattering beyond the impulse approximation, *Phys. Rev. B* **68**, 235104 (2003).
- [21] K. Suzuki, B. Barbiellini, Y. Orikasa, N. Go, H. Sakurai, S. Kaprzyk, M. Itou, K. Yamamoto, Y. Uchimoto, Y. J. Wang, H. Hafiz, A. Bansil, and Y. Sakurai, Extracting the Redox Orbitals in Li Battery Materials with High-Resolution X-Ray Compton Scattering Spectroscopy, *Phys. Rev. Lett.* **114**, 087401 (2015).
- [22] P. M. Platzman and N. Tzoar, X-ray scattering from an electron Ga, *Phys. Rev.* **139**, A410 (1965).
- [23] N. Sakai and K. Ôno, Compton Profile Due to Magnetic Electrons in Ferromagnetic Iron Measured with Circularly Polarized γ rays, *Phys. Rev. Lett.* **37**, 351 (1976).
- [24] A. Koizumi, S. Miyaki, Y. Kakutani, H. Koizumi, N. Hiraoka, K. Makoshi, N. Sakai, K. Hirota, and Y. Murakami, Study of the e_g Orbitals in the Bilayer Manganite $\text{La}_{2-2x}\text{Sr}_{1+2x}\text{Mn}_2\text{O}_7$ by Using Magnetic Compton-Profile Measurement, *Phys. Rev. Lett.* **86**, 5589 (2001).
- [25] Y. Li, P. A. Montano, J. F. Mitchell, B. Barbiellini, P. E. Mijnders, S. Kaprzyk, and A. Bansil, Temperature-Dependent Orbital Degree of Freedom of a Bilayer Manganite by Magnetic Compton Scattering, *Phys. Rev. Lett.* **93**, 207206 (2004).
- [26] J. A. Duffy, What we can learn from magnetic Compton scattering: Application to the determination of spin polarization, *J. Phys.: Conf. Ser.* **443**, 012011 (2013).
- [27] S. Kamali, K. Shih, B. Barbiellini, Y. J. Wang, S. Kaprzyk, M. Itou, A. Bansil, and Y. Sakurai, Extracting the cation distributions in $\text{NiFe}_{2-x}\text{Al}_x\text{O}_4$ solid solutions using magnetic Compton scattering, *J. Phys.: Condens. Matter* **27**, 456003 (2015).
- [28] Z. Yan, I. A. Kibalin, N. Clauser, S. Gueddida, B. Gillon, A. Gukasov, A. B. Voufack, F. Morini, Y. Sakurai, M. Brancewicz, M. Itou, M. Itoh, N. Tsuji, M. Ito, M. Souhassou, C. Lecomte, P. Cortona, and J. M. Gillet, Spin density in YTiO_3 : II. Momentum-space representation of electron spin density supported by position-space results, *Phys. Rev. B* **96**, 054427 (2017).
- [29] Y. Sakurai, High-energy inelastic-scattering beamline for electron momentum density study, *J. Synch. Radiat.* **5**, 208 (1998).
- [30] Y. Kakutani, Y. Kubo, A. Koizumi, N. Sakai, B. L. Ahuja, and B. K. Sharma, Magnetic Compton profiles of fcc-Ni, fcc- $\text{Fe}_{50}\text{Ni}_{50}$, and hcp-Co, *J. Phys. Soc. Jpn.* **72**, 599 (2003).
- [31] G. Kresse and D. Joubert, From ultrasoft pseudopotentials to the projector augmented-wave method, *Phys. Rev. B* **59**, 1758 (1999).
- [32] G. Kresse and J. Furthmüller, Efficient iterative schemes for *ab initio* total-energy calculations using a plane-wave basis set, *Phys. Rev. B* **54**, 11169 (1996).
- [33] G. Kresse and J. Hafner, *Ab initio* molecular dynamics for open-shell transition metals, *Phys. Rev. B* **48**, 13115 (1993).
- [34] J. P. Perdew, K. Burke, and M. Ernzerhof, Generalized Gradient Approximation Made Simple, *Phys. Rev. Lett.* **77**, 3865 (1996).
- [35] B. Barbiellini, E. G. Moroni, and T. Jarlborg, Effects of gradient corrections on electronic structure in metals, *J. Phys.: Condens. Matter* **2**, 7597 (1990).
- [36] I. Makkonen, M. Hakala, and M. J. Puska, Calculation of valence electron momentum densities using the projector augmented-wave method, *J. Phys. Chem. Solids* **66**, 1128 (2005).
- [37] H. Hafiz, K. Suzuki, B. Barbiellini, Y. Orikasa, V. Callewaert, S. Kaprzyk, M. Itou, K. Yamamoto, R. Yamada, Y. Uchimoto, Y. Sakurai, H. Sakurai, and A. Bansil, Visualizing redox orbitals and their potentials in advanced lithium-ion battery materials using high-resolution x-ray Compton scattering, *Sci. Adv.* **3**, e1700971 (2017).
- [38] M. Cococcioni and N. Marzari, Energetics and cathode voltages of LiMPO_4 olivines ($M = \text{Fe}, \text{Mn}$) from extended Hubbard functionals, *Phys. Rev. Mater.* **3**, 033801 (2019).
- [39] X. Liu, J. Liu, R. Qiao, Y. Yu, H. Li, L. Suo, Y.-S. Hu, Y.-D. Chuang, G. Shu, F. Chou, T.-C. Weng, D. Nordlund, D. Sokaras, Y. J. Wang, H. Lin, B. Barbiellini, A. Bansil, X. Song, Z. Liu, S. Yan, G. Liu, S. Qiao, T. J. Richardson, D. Prendergast, Z. Hussain, F. M. F. de Groot, and W. Yang, Phase transformation and lithiation effect on electronic structure of Li_xFePO_4 : An in-depth study by soft x-ray and simulations, *J. Am. Chem. Soc.* **134**, 13708 (2012).
- [40] Y. Li, P. A. Montano, B. Barbiellini, P. E. Mijnders, S. Kaprzyk, and A. Bansil, Spin moment over 10-300 K and delocalization of magnetic electrons above the Verwey transition in magnetite, *J. Phys. Chem. Solids* **68**, 1556 (2007).
- [41] A. Bansil, B. Barbiellini, S. Kaprzyk, and P. E. Mijnders, Electron momentum density and Compton profile in disordered alloys, *J. Phys. Chem. Solids* **62**, 2191 (2001).
- [42] A. Bansil, S. Kaprzyk, P. E. Mijnders, and J. Tobola, Electronic structure and magnetism of $\text{Fe}_{3-x}\text{V}_x\text{X}$ ($X = \text{Si}, \text{Ga}, \text{and Al}$) alloys by the KKR-CPA method, *Phys. Rev. B* **60**, 13396 (1999).
- [43] K. Mukai, J. Sugiyama, K. Kamazawa, Y. Ikeda, D. Andreica, and A. Amato, Magnetic properties of the chemically delithiated $\text{Li}_x\text{Mn}_2\text{O}_4$ with $0.07 \leq x \leq 1$, *J. Solid State Chem.* **184**, 1096 (2011).
- [44] See Supplemental Material at <http://link.aps.org/supplemental/10.1103/PhysRevB.100.205104> for further partial density of states and schematics of magnetic structure configurations, XRD patterns, and experimental lattice constants for various lithium concentrations.
- [45] M. Bianchini, F. Fauth, E. Suard, J.-B. Leriche, C. Masquelier, and L. Croguennec, Spinel materials for Li-ion batteries: New insights obtained by operando neutron and synchrotron X-ray diffraction, *Acta Crystallogr. B* **71**, 688 (2015).
- [46] G. E. Grechnev, R. Ahuja, B. Johansson, and O. Eriksson, Electronic structure, magnetic, and cohesive properties of $\text{Li}_x\text{Mn}_2\text{O}_4$: Theory, *Phys. Rev. B* **65**, 174408 (2002).
- [47] R. Harthoorn and P. E. Mijnders, The effect of symmetry on electron momentum distributions in solids, *J. Phys. F* **8**, 1147 (1977).

- [48] T. Chiba, Covalency effects on momentum distributions in compounds: Positron annihilation in Fe_3O_4 , *J. Chem. Phys.* **64**, 1182 (1976).
- [49] B. Barbiellini, P. E. Mijnarends, S. Kaprzyk, A. Bansil, Y. Li, J. F. Mitchell, and P. A. Montano, Extracting d -orbital occupancy from magnetic Compton scattering in bilayer manganites, *J. Phys. Chem. Solids* **66**, 2197 (2005).
- [50] N. A. Chernova, G. M. Nolis, F. O. Omenya, H. Zhou, Z. Li, and M. S. Whittingham, What can we learn about battery materials from their magnetic properties? *J. Mater. Chem.* **21**, 9865 (2011).